

DNC FILE COPY

AFGL-TR-88-0046

(O)

PRECISE PROPER-MOTION MEASUREMENT
OF SOLAR GRANULATION

AD-A205 161

LAURENCE J. NOVEMBER and GEORGE W. SIMON

DTIC
ELECTED
S 07 MAR 1989
A D

Reprinted for private circulation from
THE ASTROPHYSICAL JOURNAL, Vol. 333, No. 1, Part 1, 1988 October 1

© 1988. The American Astronomical Society. All rights reserved.

PRINTED IN U.S.A.

Unclassified
SECURITY CLASSIFICATION OF THIS PAGE

REPORT DOCUMENTATION PAGE

1a. REPORT SECURITY CLASSIFICATION Unclassified		1b. RESTRICTIVE MARKINGS													
2a. SECURITY CLASSIFICATION AUTHORITY		3. DISTRIBUTION/AVAILABILITY OF REPORT Approved for public release; Distribution unlimited													
2b. DECLASSIFICATION/DOWNGRADING SCHEDULE															
4. PERFORMING ORGANIZATION REPORT NUMBER(S) AFGL-TR-89-0046		5. MONITORING ORGANIZATION REPORT NUMBER(S)													
6a. NAME OF PERFORMING ORGANIZATION Air Force Geophysics Laboratory	6b. OFFICE SYMBOL (if applicable)	7a. NAME OF MONITORING ORGANIZATION DTIC SELECTED S 07 MAR 1989 A													
6c. ADDRESS (City, State, and ZIP Code) Hanscom AFB Massachusetts 01731-5000		7b. ADDRESS (City, State, and ZIP Code)													
8a. NAME OF FUNDING/SPONSORING ORGANIZATION	8b. OFFICE SYMBOL (if applicable)	9. PROCUREMENT INSTRUMENT IDENTIFICATION NUMBER A 61102F 2311 G3 26													
8c. ADDRESS (City, State, and ZIP Code)		10. SOURCE OF FUNDING NUMBERS PROGRAM ELEMENT NO. PROJECT NO. TASK NO. WORK UNIT ACCESSION NO.													
11. TITLE (Include Security Classification) Precise Proper-Motion Measurement of Solar Granulation															
12. PERSONAL AUTHOR(S) Laurence J. November; George W. Simon															
13a. TYPE OF REPORT REPRINT	13b. TIME COVERED FROM _____ TO _____	14. DATE OF REPORT (Year, Month, Day) 1989 February 28	15. PAGE COUNT 16												
16. SUPPLEMENTARY NOTATION Reprinted from Astrophysical Journal, Vol 333, No. 1, Part 1, Oct 1, 1988															
17. COSATI CODES <table border="1"><tr><th>FIELD</th><th>GROUP</th><th>SUB-GROUP</th></tr><tr><td></td><td></td><td>Solar granulation</td></tr><tr><td></td><td></td><td>Solar atmospheric motions</td></tr><tr><td></td><td></td><td></td></tr></table>		FIELD	GROUP	SUB-GROUP			Solar granulation			Solar atmospheric motions				18. SUBJECT TERMS (Continue on reverse if necessary and identify by block number) Solar granulation Solar atmospheric motions	
FIELD	GROUP	SUB-GROUP													
		Solar granulation													
		Solar atmospheric motions													
19 ABSTRACT (Continue on reverse if necessary and identify by block number) We describe a powerful cross-correlation technique for the precise measurement of the proper motion of tracers seen on successive images of a time series of solar granulation. The cross correlation is defined as a function of position in the image, within a spatially localized apodization window (we use a Gaussian 1"-8" in size). The time average of the spatially localized cross correlation gives a measure of the displacement that is not biased by atmospheric seeing. The window size and the seeing define the effective resolution of the vector displacement determination. We use this cross-correlation technique to analyze an 80 minute run of white-light observations made at the Sacramento Peak Vacuum Tower Telescope. Even though geometric distortion due to atmospheric seeing is instantaneously at least 10-20 times larger than the observed scale of the large-scale solar displacements, 100-1000 m s ⁻¹ , its net contribution to the 80 minute average of proper motions is RMS < 20 m s ⁻¹ . The measured vector displacements clearly show solar mesogranulation and supergranulation flows having spatial scales from 10" to 40". The measured amplitude of these flows is significantly larger than the RMS 100 m s ⁻¹ noise which we attribute principally to solar granulation evolution.															
20. DISTRIBUTION/AVAILABILITY OF ABSTRACT <input type="checkbox"/> UNCLASSIFIED/UNLIMITED <input type="checkbox"/> SAME AS RPT. <input type="checkbox"/> DTIC USERS		21. ABSTRACT SECURITY CLASSIFICATION Unclassified													
22a. NAME OF RESPONSIBLE INDIVIDUAL Richard C. Altrock		22b. TELEPHONE (Include Area Code)	22c. OFFICE SYMBOL AFGL/PHS												

PRECISE PROPER-MOTION MEASUREMENT OF SOLAR GRANULATION

LAURENCE J. NOVEMBER

National Solar Observatory/Sacramento Peak¹

AND

GEORGE W. SIMON

Air Force Geophysics Laboratory, National Solar Observatory/Sacramento Peak¹

Received 1987 October 26; accepted 1988 March 30

ABSTRACT

We describe a powerful cross-correlation technique for the precise measurement of the proper motion of tracers seen on successive images of a time series of solar granulation. The cross correlation is defined as a function of position in the image, within a spatially localized apodization window (we use a Gaussian 1"-8" in size). The time average of the spatially localized cross correlation gives a measure of the displacement that is not biased by atmospheric seeing. The window size and the seeing define the effective resolution of the vector displacement determination. We use this cross-correlation technique to analyze an 80 minute run of white-light observations made at the Sacramento Peak Vacuum Tower Telescope. Even though geometric distortion due to atmospheric seeing is instantaneously at least 10-20 times larger than the observed scale of the large-scale solar displacements, 100-1000 m/s⁻¹, its net contribution to the 80 minute average of proper motions is RMS < 20 m/s⁻¹. The measured vector displacements clearly show solar mesogranulation and supergranulation flows having spatial scales from 10" to 40". The measured amplitude of these flows is significantly larger than the RMS 100 m/s⁻¹ noise which we attribute principally to solar granulation evolution.

Subject headings: Sun: atmospheric motions — Sun: granulation

1. INTRODUCTION

Proper-motion measurement predates Doppler spectroscopy for measuring velocities in astronomical objects. In astrometry, proper-motion measurement is well defined when the identification of a star in two plates is unambiguous (Strömgren 1946); star catalogs list such measurements for most nearby stars. For the Sun, sunspots have been used as tracers to measure the solar rotation rate (Newton and Nunn 1951; Ward 1965; Howard, Gilman, and Gilman 1984).

Proper-motion measurements for continuous objects or fields of stars is somewhat less well-defined since these objects evolve in detail by changes in their constituent parts. Their proper motion can only be given as some form of average. Lindblad and Brahde (1946) inferred the proper motions of nebular objects in nearby galaxies. Simon (1967), by following the motions of individual granules within the time scale of their lifetimes, reported that granules tend to move in a systematic way and associated this large-scale movement with the supergranular convective flows (Leighton, Noyes, and Simon 1962; Simon and Leighton 1964). Duval (1980) applied cross-correlation analysis to Doppler velocity maps of the supergranulation flows to define the solar rotation rate.

Quantified proper-motion measurements of solar granulation have recently been deduced from space-based observations with the SOUP experiment on Spacelab 2 (Title *et al.* 1987; November *et al.* 1987). These results were obtained using the spatially localized cross-correlation technique described by November (1986). The SOUP proper-motion maps have revealed many new features in the quiet and active Sun: 600-1000 m s⁻¹ outflow from the penumbra and photosphere surrounding a sunspot, greatly reduced horizontal flow in a region containing numerous pores, quiet Sun mesogranulation and supergranulation horizontal convective flow fields, and vortex flows. The proper motions are found to be highly correlated with the motion of magnetic features both in direction and amplitude (Simon *et al.* 1988) and the technique promises to give insight into the foot-point evolution and twisting of solar magnetic configurations. Proper-motion measurement of the large-scale horizontal flow field provides a unique tool for the study of solar convection that has far greater potential than the conventional Doppler measurement. The line-of-sight Doppler velocity measurement gives only one component of the velocity field whereas the proper-motion measurement gives all three when one considers continuity of mass for a steady subsonic flow in a horizontally stratified compressible fluid (November *et al.* 1987).

Fortunately, proper-motion measurement is not restricted just to such seeing-free space observations. In this paper we describe a cross-correlation technique and its application to ground-based observations. The atmospheric geometric distortion adds an extra noise component that is reduced by averaging methods. The basic technique is presented in §§ II and IV. The effect on the displacement measurement caused by noise sources such as geometric distortion (atmospheric seeing and film base distortion) and blurring (atmospheric seeing) is determined theoretically in § III. A sample time series of proper-motion maps made from ground-based continuum images of solar granulation is analyzed in § V. The noise in the measurement is treated using Fourier power spectrum analysis and determined as a function of various parameters in the measurement—the time delay used for the cross

¹ Operated by the Association of Universities for Research in Astronomy, Inc., under contract with the National Science Foundation. Partial support for the National Solar Observatory is provided by the United States Air Force under a memorandum of understanding with the NSF.

correlation, the cross-correlation averaging time, and the window size. This analysis permits us to identify the noise sources and their amplitudes in the data. Some of the solar features that we identify in our sample proper-motion map are discussed in § VI along with our conclusions. However, this paper is concerned mainly with the intrinsic usefulness and viability of the technique in observations that are affected by atmospheric seeing. Thus most of the observational results and analysis relevant to the solar physics will be discussed in subsequent publications.

II. SPATIALLY LOCALIZED CROSS CORRELATION

We define proper motion as the displacement that maximizes the spatially localized cross correlation between two images of a scene separated by a sampling time delay τ that is smaller than the lifetime of tracers in the scene. The two-dimensional cross-correlation function is determined at each "locale" in the scene by multiplying an intensity product with an apodizing window $W(x)$. The spatially localized cross correlation $C(\delta, x)$ is a function of four dimensions: the two-dimensional vector displacement δ between the images, and the two-dimensional central location x of the window function. $C(\delta, x)$ is defined in terms of the intensity images $J_t(x)$ and $J_{t+\tau}(x)$ which sample the scene at the 2 times t and $t + \tau$:

$$C(\delta, x) = \int J_t\left(\xi - \frac{\delta}{2}\right) J_{t+\tau}\left(\xi + \frac{\delta}{2}\right) W(x - \xi) d\xi. \quad (1)$$

The integral is over the full area of the images, but effectively it is limited in extent by the size of the apodizing window function $W(x)$. The window size thus defines the spatial resolution of the vector displacement determination. In all the numerical examples used for this work the window was taken to be a Gaussian.

The spatially localized cross correlation defined in equation (1) slides the two intensity images symmetrically in opposite directions. Equation (1) has the symmetry that the sign of displacement δ flips upon interchange of the images J_t and $J_{t+\tau}$. Shifting the images equally and oppositely under the window ensures that the two image fields are similarly masked for each spatial displacement δ : The maximum of this cross correlation is a most reasonable definition for the motion of a tracer which undergoes evolutionary changes between successive image snapshots. This formulation is not affected adversely by contrast variations that occur over the area of the window. The images are precisely compared with the same window attenuation in each displacement δ . In Appendix A we show that our definition, equation (1), is simply related to the conventional definition for the cross correlation in which each of the images is independently masked to select the area around one spatial locale.

Before forming the cross correlation, the images must be spatially filtered to remove any large-scale components. An intensity gradient over the window biases the cross correlation to give a displacement that may not be precisely the displacement of the desired tracer. Spatial filtering to remove scales larger than the window size is a simple technique that removes gradients over the window function and can make the measurement most sensitive to the horizontal transport of a particular size of tracer, e.g., that of the granulation field. We have previously used Fourier spatial filtering successfully to remove structures large compared to the tracer (e.g., November *et al.* 1987), but a numerically simpler and equally adequate filter is the convolution of the intensity image $I(\xi)$ with the Laplacian of a Gaussian (LG). This yields the spatially filtered intensity $J(\xi)$: $J(\xi) = \mathcal{L}[I(\xi)] = I(\xi) * [\nabla^2 \exp(-\xi \cdot \xi / \gamma_s^2)]$. This convolution can be written as a sum of separable components: $J(\xi) = I(\xi) * f(\xi_x) * g(\xi_y) + I(\xi) * f(\xi_y) * g(\xi_x)$, where the one-dimensional $f(\xi) = \exp(-(\xi / \gamma_s)^2)$ and $g(\xi) = \partial^2 / \partial \xi^2 [f(\xi)]$. The direct numerical evaluation of this convolution requires fewer calculations with increasing image size than the equivalent Fourier filter and is easily implemented by direct integration on an array processor. In Figure 1 we show an intensity image and its Laplacian convolution for Gaussian full widths at half-maximum (FWHM) 0.6, 1.0, 1.4 all plotted on the same scale of contrast. The spatial filter having FWHM of 1.0 satisfactorily removes all scales except that of granulation and is the size that has been used throughout this paper. The Laplacian convolution also removes power at scales smaller than the diffraction limit to reduce noise in the proper-motion measurement. The Laplacian convolution does not bias the displacement determination; i.e., $J(\xi + \delta) = \mathcal{L}[I(\xi + \delta)]$.

In order to reduce atmospheric seeing effects, it is favorable to average the cross correlation in time before locating its maximum rather than adding individual displacement maps. The time-averaged spatially localized cross correlation $\langle C(\delta, x) \rangle_t$ is most affected by images in the time series that have the highest contrast, and we will show in § III that such averaging is an optimum statistical procedure for adding low-contrast contributions when the seeing is variable. An efficient numerical method to compute $\langle C(\delta, x) \rangle_t$, including spatial filtering by convolution with the LG, $J(x) = \mathcal{L}[I(x)]$, is deduced by rewriting equation (1) as a spatial convolution. The spatial convolution in the multidimensional x is written as the volume integral: $f(x) * g(x) \equiv \int f(\xi)g(x - \xi)d\xi$. We obtain:

$$\langle C(\delta, x) \rangle_t = \left\langle \mathcal{L}\left[I_t\left(x - \frac{\delta}{2}\right)\right] \mathcal{L}\left[I_{t+\tau}\left(x + \frac{\delta}{2}\right)\right] \right\rangle * W(x). \quad (2)$$

Each temporal sample $I_t(x)$ is spatially filtered and then multiplied by the spatially filtered sample at the fixed time delay τ at discrete spatial displacements δ . Typically, 3×3 spatial displacement positions are used corresponding to $\delta_x = 0, \pm 2$ pixels and $\delta_y = 0, \pm 2$ pixels. (The smallest spatial displacement increment that can be easily represented is 2 pixels, corresponding to a shift of one image by one pixel in one direction and a shift of the second image by one pixel in the opposite direction.) The image products are averaged in time, denoted by $\langle \rangle_t$, and the result is smoothed by convolution with the sampling window $W(x)$. We summarize schematically in Figure 2 the procedure for calculating $\langle C(\delta, x) \rangle_t$.

Interpolation in the cross correlation $\langle C(\delta, x) \rangle_t$ in δ is then performed to define the displacement, $\Delta(x)$, that locally maximizes the cross correlation in each component of δ :

$$\frac{\partial \langle C(\delta, x) \rangle_t}{\partial \delta} \Big|_{\delta = \Delta(x)} = 0. \quad (3)$$

SP Quiet and Spatially Filtered

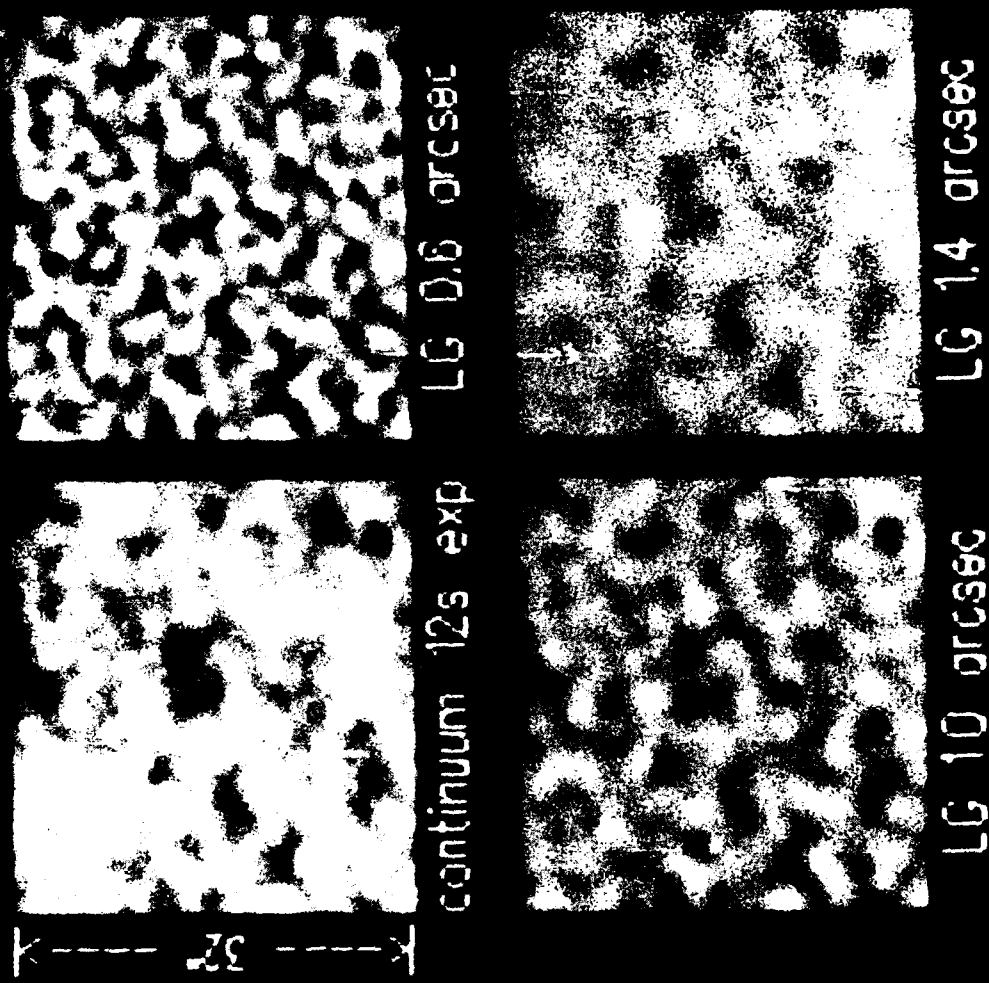


FIG. 1.—Spatial filter of solar granulation. The convolution of the image with the Laplacian of a Gaussian (LG) is a convenient spatial filter for removing large-scale intensity variations which bias the displacement measurement. An original solar granulation image (125 exposure) is shown with three spatially filtered examples all on the same scale of contrast. The scale of the spatial filter is defined by the Gaussian FWHM; the filter 1.0 was used for this work.

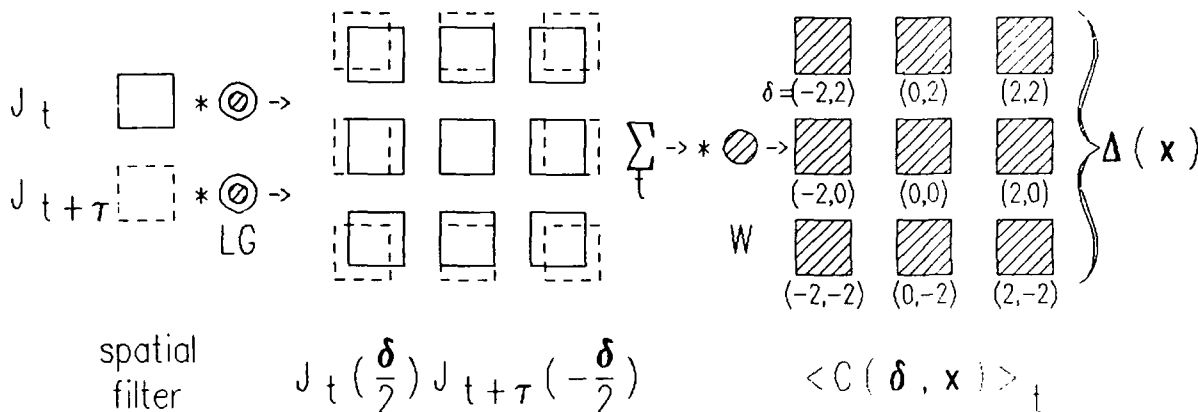


FIG. 2.—Schematic representation of the numerical method for the spatially localized cross correlation and displacement map. Two original granulation $J(x)$ images obtained at times t and $t + \tau$ are spatially filtered using the convolution with an LG. The images are shifted oppositely and multiplied at nine spatial lags to form nine cross product images which are averaged in time over the data set. The average cross product is smoothed by convolution with a Gaussian window W to form the spatially localized cross correlation $\langle C(\delta, x) \rangle$. Using a method of interpolation the maximum of the cross correlation is then determined at each position x to give the vector displacement map $\Delta(x)$.

Usually it is the case that the image displacements we wish to measure are much smaller than the distance between pixels in our digitization grid. To find an optimum interpolation method is not an insignificant task. We will discuss numerical procedures for interpolation in § IV and in Appendix C. The spatial average of displacements over the image field is taken to be zero since the exact relative motion of the image in the frame of the object is unknown.

III. EFFECT OF ATMOSPHERIC SEEING

The effect of atmospheric seeing is large in a ground-based observation, so it is important that its contribution be minimized in the average of many measurements. The instantaneous amplitude of the geometric distortion due to seeing may be as large as $0.^{\circ}2$ for solar images, even in periods of good seeing (von der Lühe 1985; November 1986), and this is at least 10–20 times larger than the amplitude of the flows we wish to measure. The obvious process of temporally averaging the time series of displacement maps does not add the contributions from the seeing noise in an optimum way when seeing conditions are variable. The local displacement is a nonlinear function of the spatially localized cross correlation and is not well defined when the granulation contrast becomes small. Since all the displacement measurements receive equal weight in the time-average displacement map, this procedure is not very satisfactory.

On the other hand, the temporal average of the spatially localized cross correlation is affected in a minimum way by the poor-seeing contributions. When the seeing is poor and the granulation contrast low, the cross-correlation peak is broad and is a nearly constant function of displacement. The poor-seeing contribution to the time-averaged cross correlation does not bias its centroid strongly and so gives a natural method for weighting contributions taken during varying seeing conditions. We consider the effect that seeing has upon the spatially localized cross correlation function in Appendix B. We summarize our conclusions from Appendix B as follows: The time-averaged spatially localized cross correlation including seeing is the cross correlation function without seeing convolved with an autocorrelation of the time-averaged seeing point-spread function. The time-averaged seeing autocorrelation is a symmetric function of displacement δ , and thus seeing tends not to bias the cross-correlation centroid. A similar cancellation of the seeing effect occurs in the displacement average when the seeing is not variable. Each image is used twice in the average: the first time an image is used the displacement error due to seeing adds, and the second time it is used, the displacement error subtracts, tending to offset the total effect. This tendency especially reduces the seeing effect in the time-averaged cross correlation because the seeing displacements tend to cancel even with varying seeing conditions.

Nevertheless, we thought it wise to average the maximum number of seeing realizations in our observations. A simple observational technique that does this is to take long exposures of the granulation field. As long as the image averaging time is smaller than the time delay τ it represents a viable sampling. The seeing effect that enters the spatially localized cross correlation made from a small number of long-exposure solar images must be the same as that made from a larger number of short-exposure images spanning the same observation period. However, the long-exposure images have a reduced granulation contrast, and provide a reduced number of independent contributions to the cross-correlation average, which further augments the loss of signal. In § V we demonstrate the viability of this procedure in a sample data set taken with 12 s exposures during a moderately good but varying seeing condition.

Another contributor to noise in the displacement determination is geometric distortion in the film base. Film-based distortion is measured to be less than $2 \mu\text{m}$ (November 1984) which corresponds to $0.^{\circ}020$ in the data analyzed in § V. In a 30 minute observing sequence, we take 108 photographic images at the 16.75 s rate. This gives RMS $0.^{\circ}0019$ which is $\sim 30 \text{ m s}^{-1}$ using a 45 s time delay τ for the cross correlation.

IV. INTERPOLATION OF $\langle C(\delta, x) \rangle$ IN δ

The cross correlation $\langle C(\delta, x) \rangle$ is defined only coarsely in the variation in the displacement δ since the product images from equation (2) can be formed only for displacements that are in discrete units of the sampling interval. A precise definition for the optimum displacement $\Delta(x)$ that maximizes the cross correlation $\langle C(\delta, x) \rangle$, equation (3), requires interpolation in δ . How closely we

are able to match interpolated $\langle C(\delta, x) \rangle$, to its actual functional form ultimately limits the precision of the displacement measurement.

In Appendix C we summarize our extensive search of interpolation methods. We obtain this general result: Methods based upon polynomials of degree less than 2 always tend to overestimate the shift for small displacements, and methods based upon polynomials of degree greater than 2 always tend to underestimate the shift. The systematic error that occurs when the degree of interpolation is other than 2 is quite large, $\sim 50\%$. Only quadratic methods give displacements correct to a precision of $\sim 10\%$.

V. NOISE ANALYSIS

We now discuss a time series of solar granulation images taken with 12 s exposure at a 16.75 s rate in continuum (5175.0 Å) at the Sacramento Peak 70 cm Vacuum Tower Telescope using the Universal Birefringent Filter UBF (Stauffer *et al.* 1983). The observations were made at disk center under moderately good but varying seeing conditions for 80 minutes beginning at 1645 UT on 1985

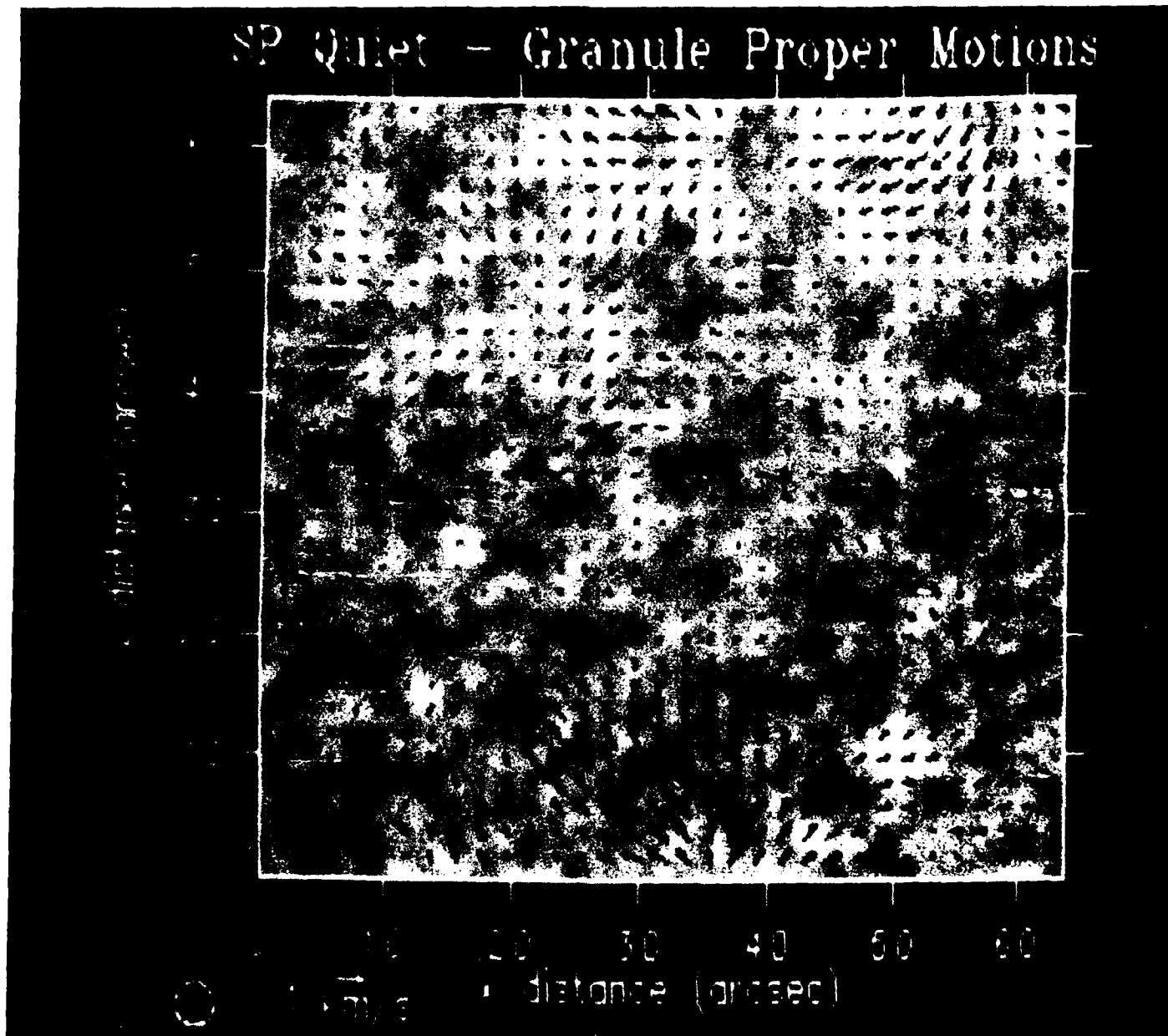


FIG. 3.—Time-averaged proper motion map of solar granulation. Vector displacements are shown superposed on a sample of the solar granulation for an 80 minute time average of the spatially localized cross correlation. Images were spatially filtered using an LG with scale 1.0 arcsec and compared with the temporal delay $\tau = 67$ s. A spatial Gaussian window of FWHM 3.3 was used as indicated by the size of the circle below the figure. The scale of the displacements is indicated by the vector below the figure.

December 29. The images were then digitized with the Sacramento Peak flying laser-spot Fast Microdensitometer (FMS) (Arrambide *et al.* 1983) in a spatial field $64'' \times 64''$ with a Gaussian spot of FWHM $0''.33$ with sampling resolution of $0''.25$. The images were spatially filtered by convolution with an LG having FWHM $1''.0$. We formed the spatially localized cross correlation using the delay $\tau = 67$ s, summing over the 80 minute observation, with the Gaussian window of FWHM $3''.3$, following equation (2) and the procedure shown in Figure 2. We used two-dimensional quadratic interpolation in $\langle C(\delta, x) \rangle$, to determine the displacements $\Delta(x)$. Figure 3 is the resulting proper-motion map. The displacements are plotted as vectors superposed on a sample granulation image from the sequence. The effective resolution of the displacement map defined by the FWHM of the window function is shown by the circle in the lower left of the figure. The scale of amplitude of the displacement vectors is shown below the figure.

We study the time series of proper motion maps from the data used for Figure 3 in order to understand the stochastic noise in the measurement. Proper-motion maps were formed from cross correlations of every third image (i.e., every 16.75 s $\times 3 \approx 50$ s) of the observations using a Gaussian window of FWHM $3''.3$ and two-dimensional quadratic interpolation. A power spectrum was made at each point in the spatial domain and in each of its two vector components by Fourier transforming the displacement measurement in the 80 minute time series of 96 proper-motion maps. The average of these power spectra is shown in Figure 4. Most of the power in the spectrum is in the DC component (frequency 0 Hz); it is off scale in the figure. For all frequencies other than DC, there are two identifiable approximately spectrally constant components: one for frequencies less than 4 mHz, and one that is evident at higher frequencies (above 7 mHz).

The standard deviation of a measurement is simply related to measurable features of its power spectrum. We discuss this relationship in Appendix D and demonstrate that the noise from an incoherent component of the signal gives contribution to the RMS according to its power. Assuming incoherence between the two spectrally constant components of Figure 4 we find that the low-frequency component, with normalized power $\sim 1.9 \times 10^4 (\text{m s}^{-1})^2$, contributes a noise of $\sim 140 \text{ m s}^{-1}$ to the measurement, while the high-frequency component with normalized power $3.6 \times 10^3 (\text{m s}^{-1})^2$, contributes noise $\sim 60 \text{ m s}^{-1}$. The power is normalized so that it represents σ_A^2 according to equation (D3).

The low-frequency component must be due mainly to the granulation which is known to be evolving on a time scale of ~ 400 s (Title *et al.* 1987). Spatial filtering attenuates the 5 minute oscillation signal in its principal scale, and averaging over many wave cycles attenuates its average signal in inverse proportion to the time, so the 5 minute oscillation will contribute much less to the solar noise than the granulation. Evolution of the large-scale flows on the time scale of the observation should also contribute to the solar noise; however, no additional component is evident in the power spectrum at the lowest frequencies. This indicates that the large-scale flows are long-lived compared to the 80 minute time of our observations.

The high-frequency component appears to be spectrally white. We suspect that it is largely caused by seeing effects and photographic granularity noise. However, a significant contribution may be solar in origin. In Figure 5 we plot the noise expressed in distance on the Sun for the two spectral components as a function of the time delay τ used in the cross-correlation determination. For this we reanalyzed the data computing an 80 minute time series of 48 proper-motion maps each formed from averaging six cross-correlation maps (100 s). This was done for different delay times τ in units of the 16.75 s sampling interval. A Gaussian window

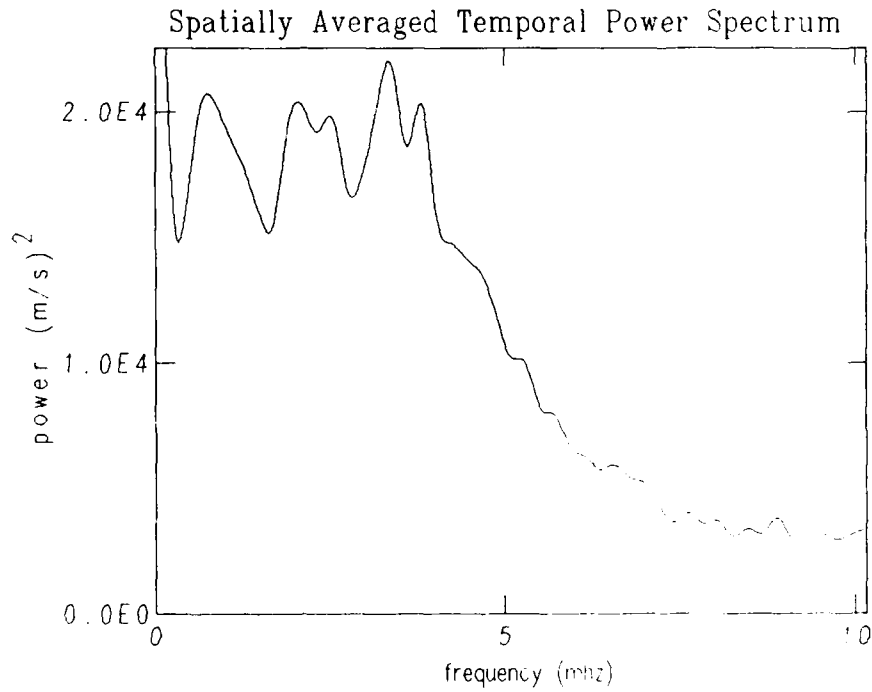


FIG. 4.—Spatially averaged temporal power spectrum of displacements

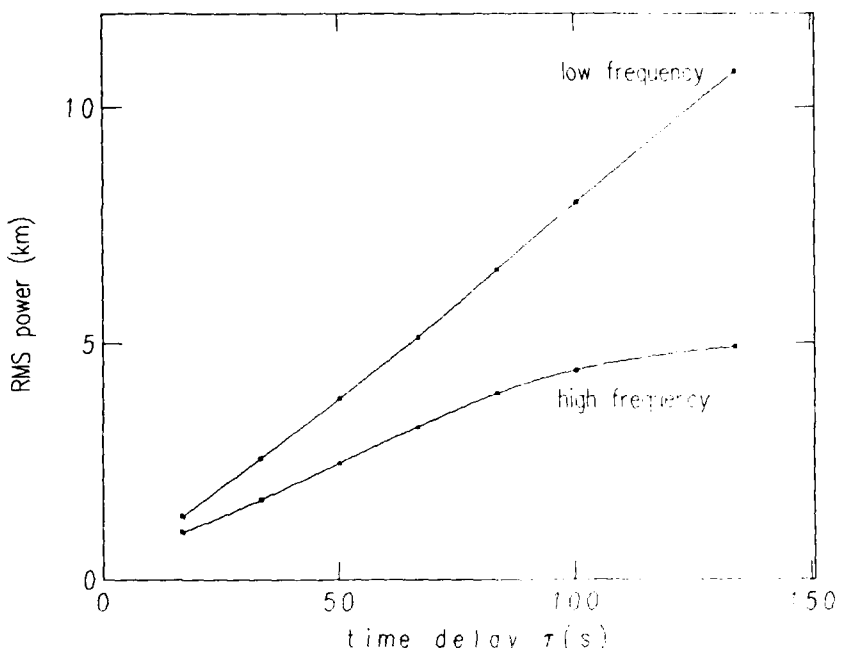


FIG. 5.—Displacement noise as a function of temporal delay. The 80 minute time series of displacement maps was formed by averaging each 50 s of cross correlation maps using the spatial filter 1°0 and the resolution window of FWHM 5" for different temporal delay times τ . The RMS power in the two identifiable spectral components from the average temporal power spectrum of Fig. 4 is shown.

of FWHM 5".0 was used for all these tests. The RMS noise is defined as the square root of the averaged normalized power in each of the two spectral components, the low-frequency ($< 5 \text{ mHz}$) and high-frequency ($> 5 \text{ mHz}$).

Detection-noise contributions (seeing and photographic granularity) should not change in RMS with the temporal delay τ , but solar-noise contributions should since the detection-noise time scale is short and the solar-noise time scale long compared to the delay time τ . The detection-noise contribution will always be the same between time samples since the 16.75 s sampling time is much greater than the time scale for the seeing. Thus the low-frequency component is not due principally to detection noise since it increases approximately linearly with the time delay τ and has zero intercept at $\tau = 0$. The high-frequency component shows a smaller increase with τ which then levels off for $\tau > 100$ s, and has a positive intercept at $\tau = 0$. A conservative estimate for the detection-noise contribution is the noise at the smallest measured delay where the solar features are least changed by structure evolution; this detection-noise contribution is 1000 m on the Sun (less than 2 milliarcsec), or 20 m s^{-1} for the time delay $\tau = 50$ s. The high-frequency component for time delays greater than 100 s must be mainly determined by those solar structures which are rapidly evolving, such as exploding granules (Title *et al.* 1987).

The displacement noise in the low-frequency component in Figure 5 increases approximately linearly with the time delay τ , indicating that the solar-noise contribution has an approximately constant signal-to-noise ratio independent of the time delay τ . Increasing the temporal baseline for the displacement measurement gives a proportional increase in the displacement signal and an approximately proportional increase in the noise due to the evolution of the tracer. In Figure 6 we show the displacement noise divided by the temporal delay. A time delay of $\sim \tau = 50$ s appears to be the best compromise to maximize an increasing signal relative to increasing noise due to tracer evolution.

The window size used for the samples in Figures 3 and 4 was 4".2 and in Figures 5 and 6 was 5".0. For a stochastic process the noise should be inversely proportional to the window size for spatial scales larger than either that of the tracer or the seeing. We plot in Figure 7 the measured velocity noise (solid line) in the low-frequency spectral component as a function of the window size for the 80 minute time series of displacement maps formed from each 100 s of data using the time delay $\tau = 67$ s. It is clear that this measured noise approaches asymptotically the expected form for a stochastic process (dashed line) as the window size is increased.

We have shown theoretically in § III that time averaging the cross correlation is a more favorable procedure than time averaging of displacement maps. Figure 8 shows the displacement RMS power of the low-frequency component from the temporal power spectra for different cross-correlation averaging times in the 80 minute data set. For each averaging time a time series of displacement maps was formed with the time delay $\tau = 67$ s and with the window size 0'.83 FWHM. The noise decreases with the averaging time and must approach a constant value for a large averaging time when the nonlinear effect of noise in the displacement determination is least. This figure indicates that little improvement can be expected from displacement maps formed from cross-correlation maps time averaged over more than ~ 5 minutes.

In earlier work we used a technique for computing proper-motion maps which applies a sonic filter to white-light granulation images before determining the displacements (Title *et al.* 1987; November *et al.* 1987). The sonic filter operates in the spatial and temporal Fourier transform domains of the data to reduce to zero the contribution having phase velocity larger than 7 km s^{-1} . By this method we eliminated this component which is due principally to the solar 5 minute oscillation. We have applied this technique to the present data set and find only small differences between the sonic-filtered map and the time-averaged proper-motion map

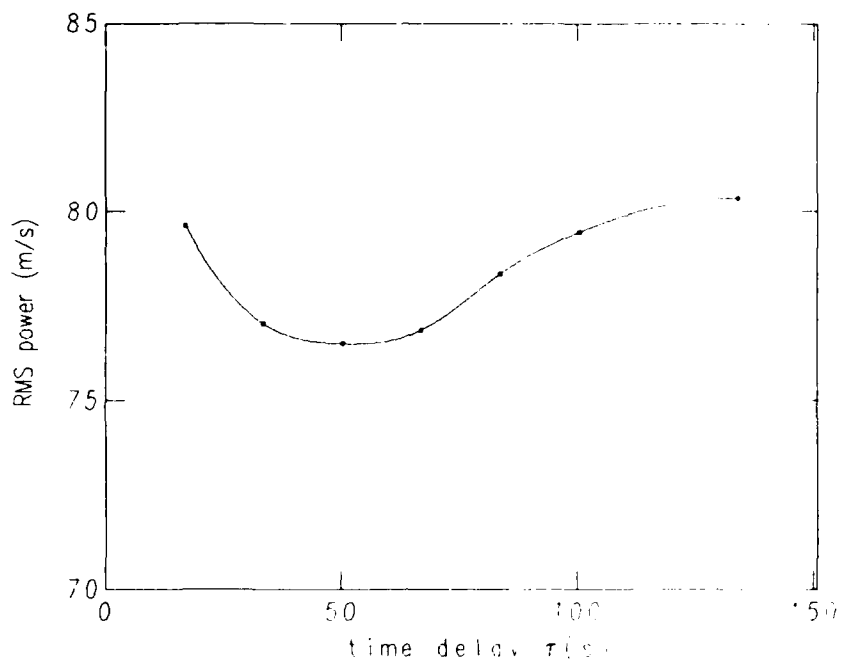


FIG. 6. Velocity noise as a function of temporal delay. The noise in displacement velocity is shown as a function of the temporal delay for the low-frequency component from Fig. 5. The signal to noise is best by a small amount when the temporal delay $\tau = 50$ s.

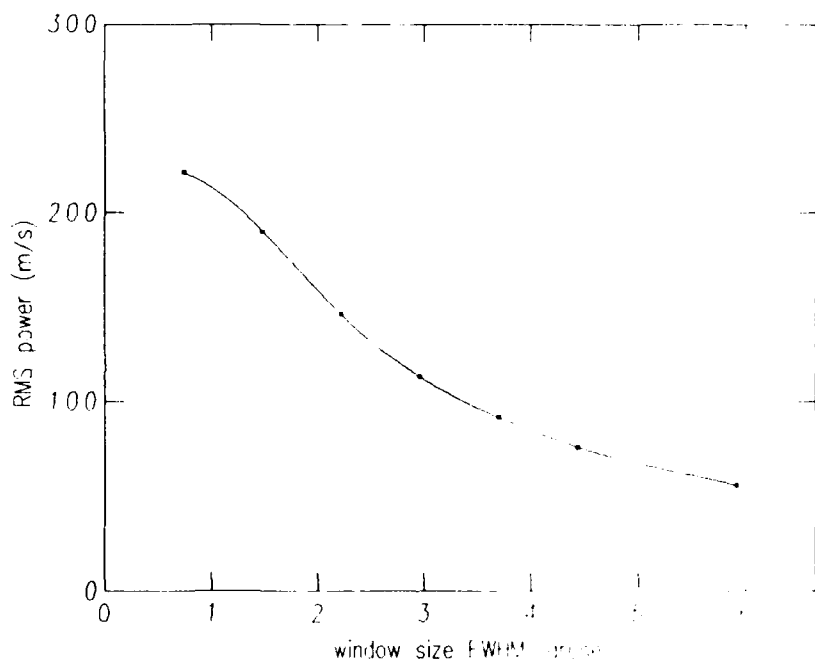


FIG. 7. Noise as a function of window size. The RMS power from the low-frequency component in the time series of displacement maps is shown (solid line) as a function of the resolution window size. For window size larger than 2" the noise approaches the form for a stochastic process varying inversely with the window size; this function is shown by the dotted line. For small window sizes the sampling is both limited by the scale of the tracer and by the seeing-disk size.

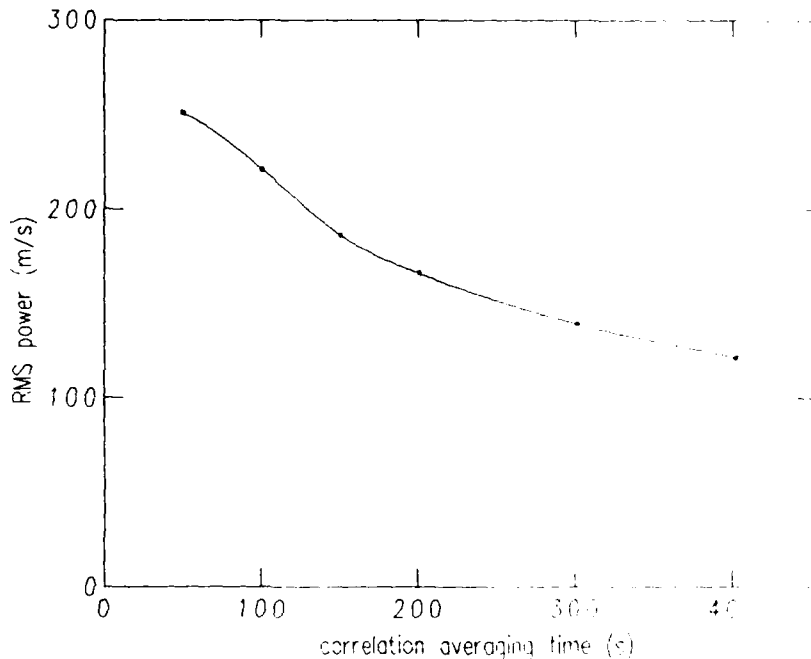


FIG. 8. Noise as a function of cross-correlation averaging time. The low-frequency contribution to the noise is shown as a function of the averaging time used in the spatially localized cross correlation for the displacement maps from the 80 minute time series. The spatial filter was $1''\text{.}0$, the temporal delay $\tau = 67\text{ s}$, and the resolution window size FWHM $0''\text{.}83$.

(Fig. 3). The temporal power spectrum of the displacements is similar to the one we show in Figure 4 in its low frequencies but significantly attenuated in its high frequencies. This is expected as the spatial filtering of the data by the convolution with an LG selects a specific range of wavenumber. In this range a specific cutoff frequency is defined by the sonic filter. The sonic filter does not change the actual noise but only serves to extinguish all the temporal variations in the displacement map time series above the cutoff frequency. In effect, sonic filtering is not different from simply time averaging the cross correlation, or time averaging the displacement maps. It therefore serves no useful purpose in our analysis and will not be used in future investigations.

VI. CONCLUSIONS

We conclude that proper motions of large-scale solar features can be determined reliably from long-exposure-time ground-based observations of solar granulation taken in moderately good but varying seeing conditions. The main effect that atmospheric seeing has on the displacement measurement is to reduce the contrast in the time-averaged spatially localized cross correlation without biasing its central displacement. The reduced contrast increases the detection noise in the measurement but is much smaller than the noise introduced by granulation evolution. In an 80 minute average with $5''$ resolution and with the optimum delay of 50 s there is $\sim 75\text{ m s}^{-1}$ noise due to tracer evolution compared to less than 20 m s^{-1} detection noise.

We are now obtaining 15 s exposure full-disk observations of the Sun in white light through a 6 inch aperture telescope. In times of poor seeing, even though the intergranular lanes are not resolved, $\sim 1\%$ granulation contrast is apparent everywhere on the disk. We are optimistic that this experiment will be able to provide full-disk proper-motion maps of selected solar features or of the full disk on a regular patrol basis.

A large-scale displacement map from our data is shown in Figure 9. The proper-motion map shown earlier (Fig. 3) lies within this larger field, as shown by the interior box. The flows in the figure appear to be long-lived relative to the 80 minute averaging time, based upon the power spectrum analysis of the time series. We identify the coordinates of a number of flow sources of amplitude $500\text{--}1000\text{ m s}^{-1}$: $(x, y) = (70, 23), (15, 80), (55, 120), (125, 43), (100, 12), (100, 108)$. We associate these radial outflows with the $40''$ supergranulation (Leighton *et al.* 1962).

In Figure 9 there is also much fine structure in the horizontal flows. This is particularly evident in the divergence of the displacements $\nabla \cdot \Delta(x)$ which we plot in Figure 10. Note that positive and negative contours in Figure 10 correspond to regions of outflow and inflow in Figure 9, respectively. The contour interval is $5 \times 10^{-5}\text{ s}^{-1}$, and the zero contour is not shown. The fine structure has a smaller scale of $10''\text{--}15''$ and appears superposed on the larger flows; we associate this with mesogranulation (November *et al.* 1981). Figure 11 shows a corresponding contour plot of the vorticity of the flows. The amplitude of the vorticity is roughly comparable to that of the divergence but the features are generally uncorrelated. The cyclonic flows we identify here must be convective in origin. These data are for Sun center; Coriolis-induced flows remain a possibility for high latitudes. The time scales for the flows is longer than the 80 minute time average for the displacement map. We are now investigating the distribution of size scales, the relation of these flows to Doppler velocity and longitudinal magnetic field observations of the Sun, the temporal evolution of the flow morphology, the fluid vorticity and divergence relation for the Coriolis effect in the convection cells, and the effective angular momentum transport over the Sun's surface in these scales of motion. We will discuss these issues in future publications.

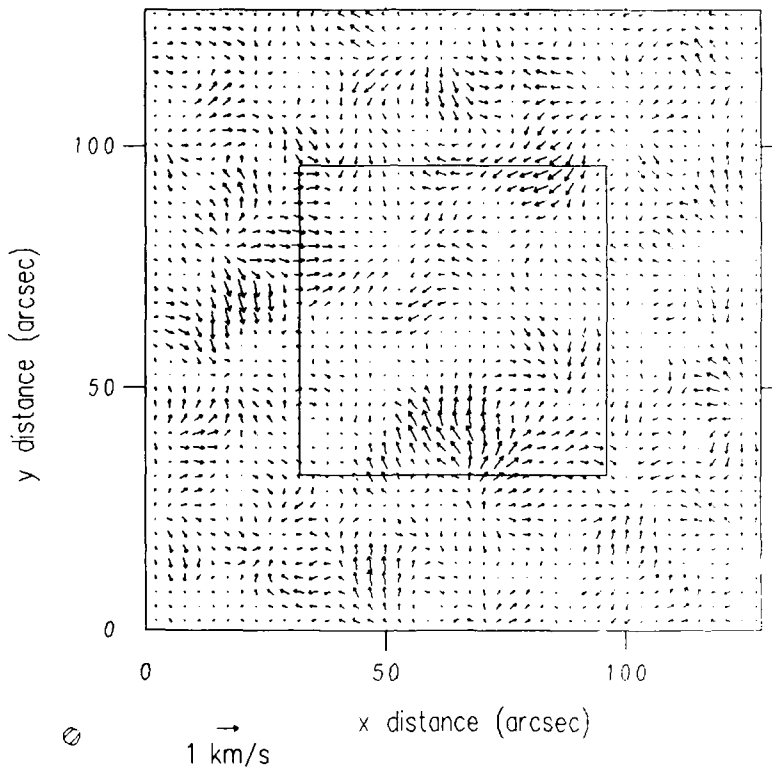


FIG. 9.—Proper-motion map of a portion of the solar image. It was formed from the 80 minute time average of the spatially localized cross correlation using the spatial filter $1''0$, the temporal delay $\tau = 67$ s, and the resolution window $3''3$. The scale of the displacements is shown below the figure. This map contains the smaller map (Fig. 3) as indicated by the enclosed box. We associate the largest amplitude flows with the supergranular horizontal convective motion.

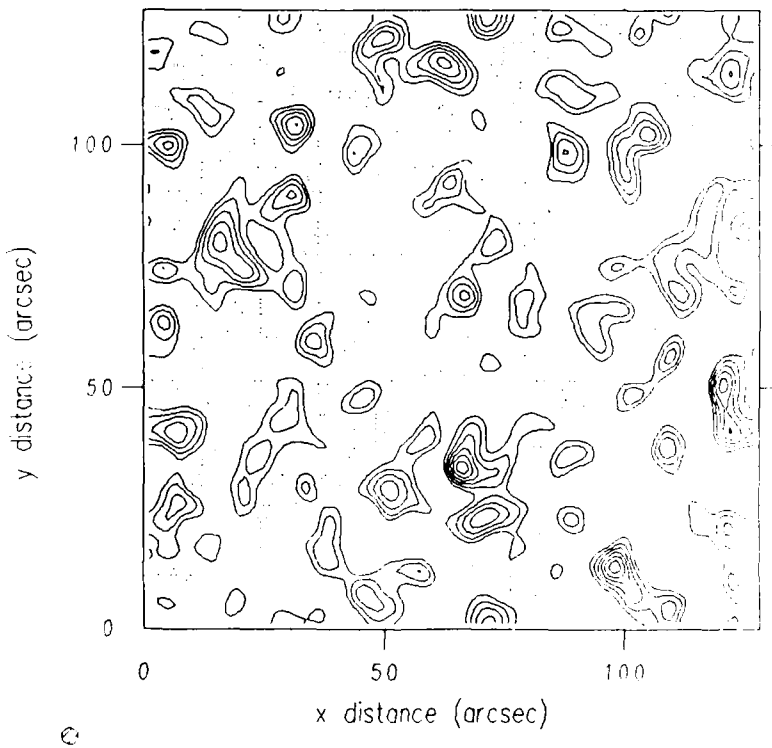


FIG. 10.—Divergence of flows. The divergence is defined $\nabla \cdot \Delta(x)$. Contours are plotted at intervals of $5 \times 10^{-5} \text{ s}^{-1}$, positive as solid line, negative as dashed line for the 80 minute average from Fig. 9 (the zero contour is not shown). The typical size scale in this map is $10'' 15''$, corresponding to the scale of mesogranulation.

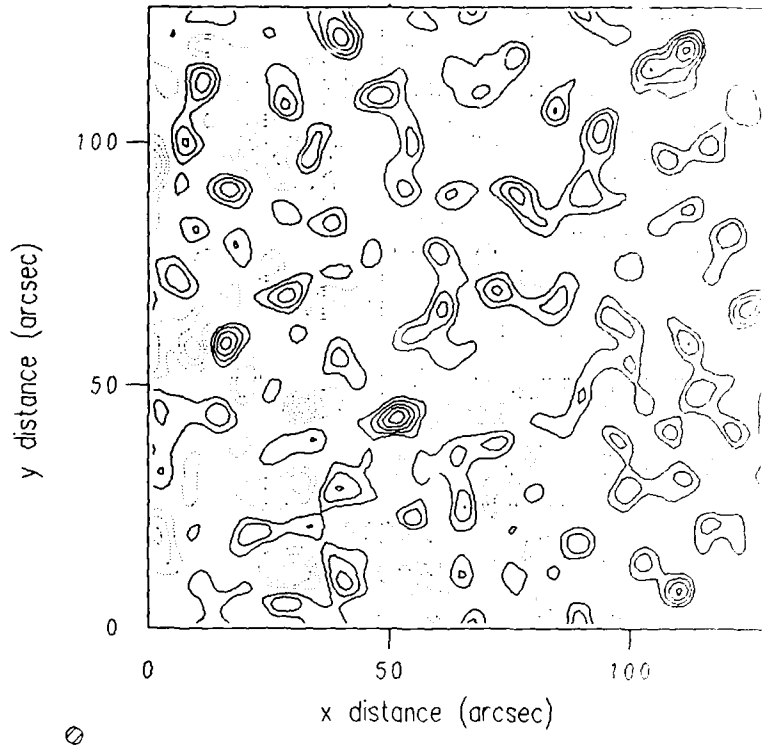


FIG. 11.—Vorticity of Flows. The vorticity is defined as $\partial \Delta_y(x)/\partial x - \partial \Delta_x(x)/\partial y$. Contours are plotted at intervals of $5 \times 10^{-5} \text{ s}^{-1}$, positive as solid line, negative as dashed line for the 80 minute average from Fig. 9 (the zero contour is not shown). The typical size scale in the vorticity is also $10''-15''$.

We note in closing that two other high-resolution ground-based time series of solar granulation are currently being analyzed using techniques similar to those described herein. One uses the Swedish Vacuum Solar Telescope at La Palma (Brandt *et al.* 1988), and the other the Sacramento Peak Vacuum Tower Telescope (Title *et al.* 1988). One of their preliminary results, as in this work and in the SOUP observations, is that mesogranulation is a dominant large-scale flow feature on the solar surface.

One of us (I. J. N.) initiated a study in techniques for proper-motion analysis of tracers in 1982 in collaboration with R. Dunn and R. Petrov. The method was first applied successfully in a collaboration between us and T. Tarbell, S. Ferguson, and A. Title in the analysis of Spacelab 2 SOUP observations in 1986. Tarbell also demonstrated to us the usefulness of Fourier techniques for noise analysis of proper-motion measurements.

APPENDIX A

$C(\delta, x)$ THE CONVENTIONAL CROSS CORRELATION

Our definition for the spatially localized cross correlation, $C(\delta, x)$ from equation (1), when multiplied by an attenuation factor in δ , $W''(\delta/2)$, is algebraically equivalent to the conventional definition for the cross correlation of two images in which each is independently masked to select one locale:

$$\int J_1\left(\xi - \frac{\delta}{2}\right) J_{1+\epsilon}\left(\xi + \frac{\delta}{2}\right) W(x - \xi) \partial\xi W''\left(\frac{\delta}{2}\right) = \int J_1(\xi) J_{1+\epsilon}(\xi + \delta) W(x - \xi) W''(x - \xi - \delta) \partial\xi. \quad (\text{A1})$$

If $W'(x)$ is a Gaussian then $W(x)$ and $W''(x)$ are also Gaussians having width $2^{1/2}$ the width of $W'(x)$. For the general window function $W'(x)$ we find $\bar{W}(k_1)\bar{W}''(k_2) = \bar{W}'[\frac{1}{2}(k_1 + k_2)]\bar{W}''[\frac{1}{2}(k_1 - k_2)]$ where $\bar{W}(k)$ is the Fourier transform of $W'(x)$; $\bar{W}'(k) = \int W'(x) \exp(-ik'x) dx$, and $\bar{W}(k)$ and $\bar{W}''(k)$ are the Fourier transforms of the window function $W'(x)$ and $W''(x)$, respectively. (Herein we always use the overbar to denote the Fourier transform.) This result is found by substituting Fourier integrals for the window function $W'(x)$ in equation (A1) and changing variables of integration. When the real window function $W'(x)$ is chosen to have unit area, then $\bar{W}(k) = \bar{W}'(k) = \bar{W}'(\frac{1}{2}k)^2$. The conventional definition for the cross correlation acting on images that are separately masked, equation (A1), gives a slightly different measurement of the displacement than our spatially localized cross correlation $C(\delta, x)$. The difference is a displacement bias caused by the finite extent of the window $W''(\delta/2)$. Equation (1) gives a more accurate displacement measure because the image fields are unbounded in x as they are shifted in opposite directions under the fixed sampling window $W'(x)$.

APPENDIX B

THE EFFECT OF SEEING ON $\langle C(\delta, x) \rangle_t$

We demonstrate here that seeing represented by a slowly spatially varying point-spread function in the object $O_i(x)$ has the effect of convolving the time-averaged spatially localized cross correlation $\langle C(\delta, x) \rangle_t$ with a symmetric function in δ . The seeing function is assumed to be uncorrelated with the seeing function displaced in time by the time delay τ for the cross correlation, and uncorrelated with the scene. We also assume that the time-averaged seeing function is spatially homogeneous and that the averaging time is long compared to the time delay τ .

Let the instantaneous effect of seeing on the solar-granulation intensity field $O_i(x)$ be represented by the following convolution: $I_i(x) = \int S_i(\xi, x) O_i(x - \xi) d\xi$. The instantaneous seeing point-spread function $S_i(\xi, x)$ is allowed to vary slowly in x over the image. The associativity property of the normal convolution allows separation of the spatial filter: $\mathcal{L}[I_i(x)] = \int S_i(\xi, x) \mathcal{L}[O_i(x - \xi)] d\xi$. The result is formally shown for the slowly spatial-varying seeing point-spread function by writing $\mathcal{L}[I_i(x)]$ as an integral, making a substitution of the variable of integration, and noting that the spatial scale of the Gaussian in the integral (in this case taken to be the scale of the solar granulation) is small compared to the scale of spatial variation of the seeing point-spread function. Thus we have for $\langle C(\delta, x) \rangle_t$, from equation (2):

$$\langle C(\delta, x) \rangle_t = \int \left\langle \mathcal{L}\left[O_i\left(\xi_1 - \frac{\delta}{2} - \xi_2\right)\right] \mathcal{L}\left[O_{i+\tau}\left(\xi_1 + \frac{\delta}{2} - \xi_3\right)\right] W(x - \xi_1) S_i(\xi_2, x) S_{i+\tau}(\xi_3, x) \right\rangle d\xi_1 d\xi_2 d\xi_3, \quad (B1)$$

where ξ_1 , ξ_2 , and ξ_3 are variables of integration.

The time average of a product of incoherent components is the product of the time averages of each of those components. Mutual incoherence is a reasonable physical approximation between the seeing point-spread functions S_i and $S_{i+\tau}$, and the correlation function $\mathcal{L}[O_i] \mathcal{L}[O_{i+\tau}]$. It is generally believed that the seeing cannot be correlated for time scales longer than 1 s, and in this analysis the time delay τ is much larger, of order 1 minute. Thus the seeing fluctuations and the image product must be uncorrelated, and we may rewrite equation (B1) as

$$\langle C(\delta, x) \rangle_t = \int \left\langle \mathcal{L}\left[O_i\left(\xi_1 - \frac{\delta}{2} - \xi_2\right)\right] \mathcal{L}\left[O_{i+\tau}\left(\xi_1 + \frac{\delta}{2} - \xi_3\right)\right] \right\rangle W(x - \xi_1) \langle S(\xi_2) \rangle_t \langle S(\xi_3) \rangle_t d\xi_1 d\xi_2 d\xi_3; \quad (B2)$$

$\langle S(\xi) \rangle_t$ denotes the time-averaged seeing point-spread function which must be the same in the time average $\langle S_i \rangle_t$ and in the temporally displaced time average $\langle S_{i+\tau} \rangle_t$ in the limit that the averaging time is long compared to the temporal delay τ . Also, we assume that the time-averaged seeing point-spread function does not vary over the spatial domain of the image, which must always be true in the long-time average.

The integral is reduced by substituting Fourier integrals for each of the functions: $\mathcal{L}[O_i(x)] = \int \bar{O}_i \exp(ik \cdot x) dk$, $W(x) = \int \bar{W}(k) \exp(ik \cdot x) dk$, $\langle S(\xi) \rangle_t = \int \langle \bar{S}(k) \rangle_t \exp(ik \cdot \xi) dk$. Of course, the functions $\bar{O}_i(k)$, $\bar{W}(k)$, and $\langle \bar{S}(k) \rangle_t$ are defined as the negative-signed- i Fourier integrals of the variables $\mathcal{L}[O_i(x)]$, $W(x)$, $\langle S(\xi) \rangle_t$, respectively; $\langle \bar{S}(k) \rangle_t$ is the temporally averaged seeing modulation-transfer function. After substitution and rearrangement of the terms in equation (B2), δ -function integrals occur which simplify the integral and give the following Fourier integral for $\langle C(\delta, x) \rangle_t$ over the two wavenumber variables k_x and k_δ :

$$\langle C(\delta, x) \rangle_t = \int \langle \bar{O}_i(\frac{1}{2}k_x + k_\delta) \rangle_t \langle \bar{O}_{i+\tau}(\frac{1}{2}k_x - k_\delta) \rangle_t \bar{W}(k_x) \langle \bar{S}(\frac{1}{2}k_x + k_\delta) \rangle_t \langle \bar{S}(\frac{1}{2}k_x - k_\delta) \rangle_t e^{ik_\delta \cdot \delta} e^{ik_x \cdot x} dk_\delta dk_x. \quad (B3)$$

It is useful to write this Fourier transform as a convolution in the spatial variables δ and x [i.e., $f(\delta, x) * g(\delta, x) \equiv \int f(\epsilon, \xi) g(\delta - \epsilon, x - \xi) d\epsilon d\xi$]:

$$\begin{aligned} \langle C(\delta, x) \rangle_t = & \int \langle \bar{O}_i(\frac{1}{2}k_x + k_\delta) \rangle_t \langle \bar{O}_{i+\tau}(\frac{1}{2}k_x - k_\delta) \rangle_t \bar{W}(k_x) e^{ik_\delta \cdot \delta} e^{ik_x \cdot x} dk_\delta dk_x \\ & * \int \langle \bar{S}(\frac{1}{2}k_x + k_\delta) \rangle_t \langle \bar{S}(\frac{1}{2}k_x - k_\delta) \rangle_t e^{ik_\delta \cdot \delta} e^{ik_x \cdot x} dk_\delta dk_x. \end{aligned} \quad (B4)$$

The first integral in equation (B4) is the spatially localized cross correlation without seeing; it is convolved in (δ, x) with the seeing-function integral, an integral that is defined entirely by the time-averaged seeing point-spread function. The product $\langle \bar{S}(\frac{1}{2}k_x + k_\delta) \rangle_t \langle \bar{S}(\frac{1}{2}k_x - k_\delta) \rangle_t$ in the seeing-function integral is invariant with the change of sign of k_δ so that the sine integral due to $\exp(ik_\delta \cdot \delta)$ is zero. Thus the seeing-function integral is a symmetric function of δ for all k_x . This proves that seeing has the effect of smoothing the spatially localized cross correlation in δ by convolution with a symmetric function. The convolution cannot change the centroid of the cross correlation in δ but may only change its shape; i.e., broaden the cross correlation.

In principle, seeing might introduce a location error for the displacement since the seeing-function integral in equation (B4) is not necessarily symmetric in x . However, if $\langle S(\xi) \rangle_t$ is a symmetric function, and real by definition, then $\langle \bar{S}(k) \rangle_t$ is real and symmetric, and the seeing-function integral is also symmetric in x . We note that the convolution of the spatially localized cross correlation in x has the effect of changing the shape of the window function. Thus seeing can reduce the effective spatial resolution of the displacement map.

If the time-averaged seeing point-spread function $\langle S(\xi) \rangle_t$ is a Gaussian, then the spatial and displacement convolutions become

separable in the seeing-function integral of equation (B4). If $\langle S(\xi) \rangle_t$ is a Gaussian then $\langle \tilde{S}(k) \rangle_t$ is also a Gaussian and the product $\langle \tilde{S}(\frac{1}{2}k_x + k_s) \rangle_t \langle \tilde{S}(\frac{1}{2}k_x - k_s) \rangle_t$ is the product of a Gaussian in k_x and a Gaussian in k_s . The spatially localized cross correlation from equation (B4) is the spatially localized cross correlation without seeing, convolved in δ with a Gaussian, and then convolved in x with the product of a Gaussian and a window function.

The result that the time-averaged seeing integral is a symmetric function of displacement δ is a direct consequence of the fact that each image is used twice in forming the average, once at time t and again at time $t + \tau$. The first time an image is used, the displacement error due to seeing adds, and the second time the image is used, the displacement error subtracts, canceling its total effect. The cancellation of the displacement error negates the effect of geometric distortion in the time-averaged cross correlation in the limit that the averaging time is long compared to the time delay τ for the cross correlation.

APPENDIX C

INTERPOLATION IN $C(\delta, x)$

The precision of a displacement measurement is limited by the accuracy of the spatial interpolation technique used. We were surprised to learn, after trying several methods, that this accuracy varies widely with the method, and has a very significant effect on the result. Thus we undertook an extensive investigation of interpolation techniques, which we describe here.

We base our empirical tests on interpolation techniques upon digital images made from one photographic sample of solar granulation. The photograph was scanned with positional centers that were displaced by different fractions of a pixel. The images were digitized with the Sacramento Peak FMS. The FMS has a spatial resolution of $0.^{\circ}025$ in the scale of the photographic sample with positional accuracy $0.^{\circ}003$ mas (± 0.1 pixel). Two digital images with centers displaced by 0.1 pixel were made from a field of granulation $64'' \times 64''$ using a Gaussian spot of FWHM $0.^{\circ}5$ with a sampling increment $0.^{\circ}25$. The digital images were cleaned to remove dust and other artifacts using a numerical method (November 1988).

One of the digital images was shifted by interpolation to a new image center and compared to the other image. Figure 12 shows the RMS of the difference of the images as a function of the interpolation shift for different degrees of a polynomial interpolation. We see that the degree 3 polynomial (cubic) gives by a slight margin the minimum RMS difference. For the smallest interpolation degrees, there is best agreement with the offset digitized image when a displacement greater than the true shift is used for the interpolation. We say that the lower degree methods systematically overestimate the actual shift by as much as 10% for small shifts. The higher degree (greater than 5) methods systematically underestimate the actual shift by as much as 40% for small shifts.

Other methods of interpolation behave similarly: two-dimensional cubic splines through 9×9 points, one-dimensional cubic convolution in 4×4 points, and two-dimensional quadratic interpolation in 3×3 points (six-point and nine-point formulas) all tend to overestimate the actual shift by 10%–25%. The interpolation shift error is found to be fairly independent of the sample size.

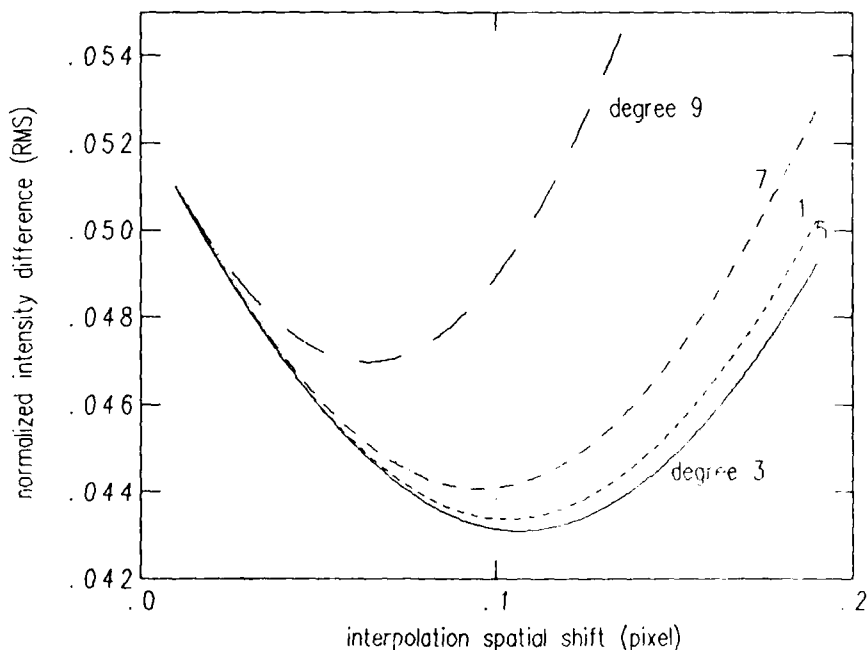


FIG. 12.—Accuracy of images artificially shifted by five methods of interpolation. The normalized RMS difference between two images which were digitized with their centers offset by 0.1 pixel is plotted as a function of the interpolation spatial shift that was applied to one of the images for various degrees of polynomial interpolation. The scale of the RMS was normalized by the RMS image contrast.

or the sampling interval as long as the solar granulation is properly resolved. However, the systematic error is noise sensitive: if we use low-pass spatially filtered images, then the higher order methods less severely underestimate the shift than in the unfiltered examples shown in Figure 12.

Fourier interpolation should give an exact result since, by the Fourier theorem, a function that is band-limited is exactly represented by a finite number of Fourier sine and cosine terms. In practice, however, Fourier interpolation is most sensitive to sampling effects. We find that when the image shift is near $\frac{1}{2}$ pixel its RMS variance with the digitized offset image is several times larger than errors typical of the local interpolation methods. Fourier interpolation methods have to be rejected as unsuitable for accurate displacement measurements.

Our result, that interpolation may shift erroneously an image by a significant amount, warns of the danger in using interpolation to estimate the extreme position of a function. To analyze these methods further, we digitized along the 45° diagonal the sample granulation photograph at 12 evenly spaced offset positions separated by 0.1414 pixel. The digitized images were numerically cleaned and spatially filtered. The spatially localized cross correlations $C(\delta, x)$ was computed between each offset digitized image and the undisplaced digitized image with a Gaussian window of FWHM $3''3$ in 3×3 offsets δ of $\delta_x = 0, \pm 2$ and $\delta_y = 0, \pm 2$ pixels. A solution for the extremum position, the displacement $\Delta(x)$, is given in the 3×3 array of $C(\delta, x)$ at each x by the least-squares fit in a two-dimensional quadratic function with 6 degrees of freedom. In Figure 13 we show the spatial x average of displacements normalized by the digitization offset as a function of the digitization offset for each offset digitized image compared to the undisplaced digitized image. The spatial average of displacements is plotted as a point with error bars at $\pm 1\sigma$. The accuracy of the method is $\sim 10\%$ for digitization offsets less than 1 pixel (the relevant range of offsets for this work). A similar test made of an image field containing a large sunspot shows similar accuracy and noise; this demonstrates the viability of the method even in a field containing large changes of structure and feature contrast.

We show in Figure 14 the spatially averaged displacement as a function of the digitization offset for three different methods of interpolation. The solid line is for the quadratic interpolation from Figure 13. The dashed line gives the estimated displacement using a method of linear interpolation in 3×3 points, while the dotted line is the estimated displacement using a polynomial of degree 4 (quartic) fit through 5 spatial points in each direction in δ . We have tried other orders of polynomials in two-dimensional and in one-dimensional separable forms fit through varying numbers of points, as well as other methods including two-dimensional cubic splines and one-dimensional separable cubic convolution.

In summary, our investigation gives this general result: Methods based upon polynomials of degree less than 2 always tend to overestimate the shift for small displacements, and methods based upon polynomials of degree greater than 2 always tend to underestimate the shift. The systematic error that occurs when the degree of interpolation is other than 2 is quite large, $\sim 50\%$. Only quadratic methods give displacements correct to a precision of $\sim 10\%$.

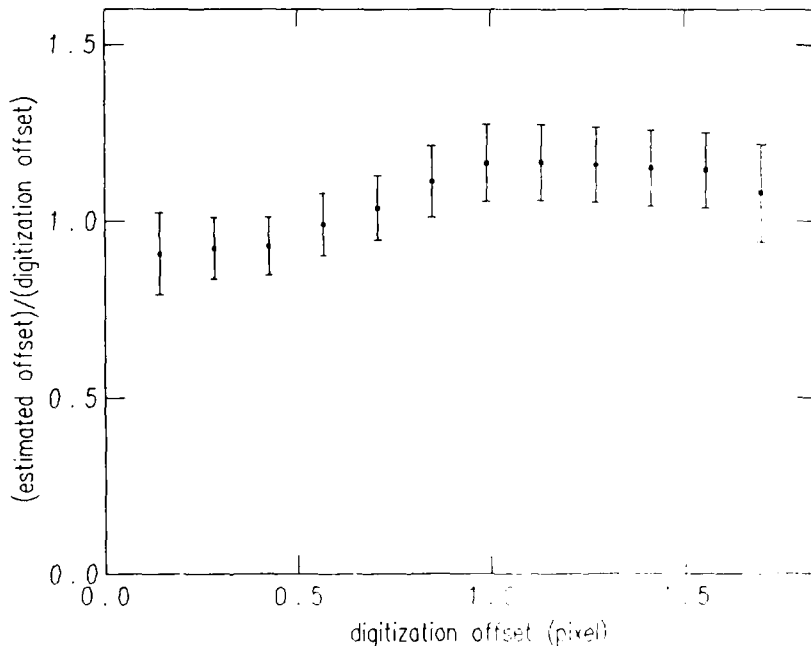


FIG. 13.—Precision of displacement measurement using quadratic interpolation. Images of a scene of solar granulation were digitized at 12 positions in increments of 0.1 pixel and displacement maps formed by comparison with the unshifted image. Average of displacements over the area of each displacement map is shown with error bars representing $\pm 1\sigma$. The points are normalized by the digitization offset and plotted as a function of digitization offset.

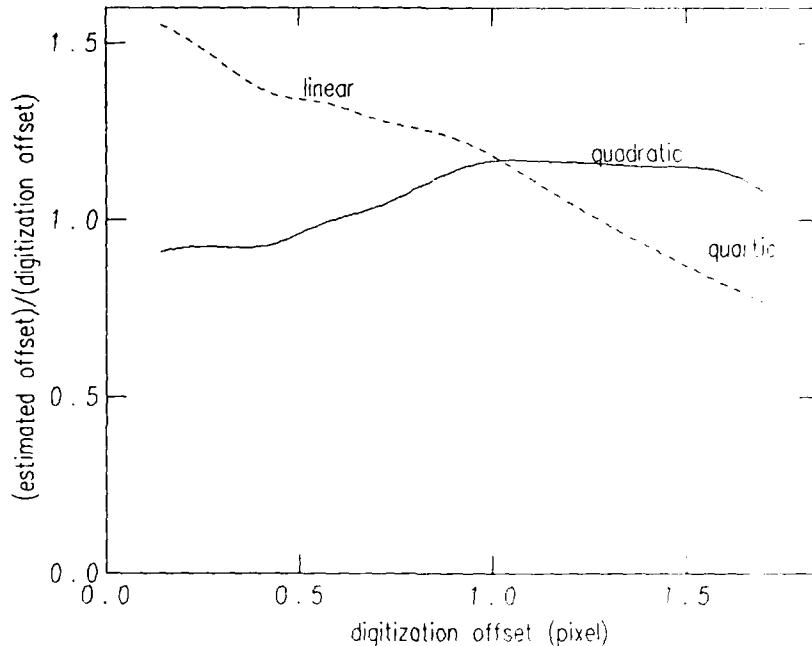


FIG. 14.—Comparison of interpolation methods. The spatial average of displacements normalized by the digitization offset is shown as a function of the digitization offset between image samples made of a common scene of solar granulation using three methods of interpolation in the spatially localized cross correlation. Interpolation by two-dimensional quadratic (solid line) gives the most precise measurement. Interpolation by a two-dimensional linear function (dashed line) in the 3×3 spatially localized cross correlation and interpolation by separable quartic polynomial (dotted line) in the 5×5 spatially localized cross correlation are also shown.

APPENDIX D

NOISE ESTIMATION BY POWER-SPECTRUM ANALYSIS

The standard formula for the temporal RMS standard deviation σ_A of the signal $\Delta(t)$ is $\sigma_A^2 = \langle \Delta(t)^2 \rangle_t - \langle \Delta(t) \rangle_t^2$, where $\langle \rangle$ denotes the time-averaged quantity. This formula is valid in the special case when the samples are independent and randomly distributed about the average signal.

A more general definition for the standard deviation that considers the possibility that samples may not be independent is given from power spectral analysis of the signal $\Delta(t)$. Let $\bar{\Delta}(\omega)$ be the Fourier transform of $\Delta(t)$. Then by the Fourier power theorem we have for $\bar{\Delta}(\omega)$:

$$\int \bar{\Delta}(\omega) \bar{\Delta}(\omega)^* d\omega = \int \Delta(t)^2 dt. \quad (D1)$$

The integrals are over the two domains frequency ω and time t . Let us write $\Delta(\omega)$ as a superposition of mutually incoherent signal components: $\bar{\Delta}(\omega) = \sum_j \bar{\Delta}_j(\omega)$; the summation is over the index j which counts individual signal components. We identify a special DC component which is the signal integral, $\bar{\Delta}_0 \equiv T \langle \Delta(t) \rangle_t$, where T is the length of the time domain. It is zero at all frequencies $\omega \neq 0$. The DC component is incoherent with respect to the fluctuating components if and only if the fluctuating components are randomly distributed. This condition is usual for a noise signal which fluctuates about an average. This assumption of incoherence between the DC component and the fluctuating element $\bar{\Delta}_j(\omega)$ is written: $\langle \bar{\Delta}_0 \bar{\Delta}_j(\omega) \rangle_\omega = 0$. The assumption of incoherence among all the other individual elements obeys the same rule: $\langle \bar{\Delta}_j(\omega) \bar{\Delta}_k(\omega) \rangle_\omega = 0$ for all $j \neq k$. Substituting the summation of incoherent components for $\bar{\Delta}(\omega)$ into equation (D1) gives:

$$\sum_{j=1}^n \int \bar{\Delta}_j(\omega) \bar{\Delta}_j(\omega)^* d\omega = T(\langle \Delta(t)^2 \rangle_t - \langle \Delta(t) \rangle_t^2). \quad (D2)$$

We have subtracted the squared DC component written as a time average from both sides of equation (D1) and rewritten the integral in time as an average to give equation (D2). The summation counts n incoherent elements in addition to the DC that we have identified for the system.

We recognize the difference of averages on the right side of equation (D2) which is the usual formula for σ_A^2 for special cases.

Equation (D2) suggests the following as a more general definition for σ_{Δ}^2 :

$$\sigma_{\Delta}^2 = \frac{1}{T} \sum_{j=1}^n \int \bar{\Delta}_j(\omega) \bar{\Delta}_j(\omega)^* d\omega . \quad (\text{D3})$$

Consider now the usual special case that the spectrum contains two incoherent components, the DC component $\bar{\Delta}_0$ and a spectrally white component $\bar{\Delta}_1(\omega)$. The spectrally white component is constant in frequency for all frequencies up to the Nyquist sampling frequency ω_N . The integral in frequency must be taken from $-\omega_N$ to $+\omega_N$ and the right side of equation (D3) becomes the constant power $|\bar{\Delta}_1|^2$ divided by the number of samples, $2T\omega_N$, using the definition for the Nyquist frequency. But from the power theorem, the power in the white component is simply the integrated signal for discrete samples: $|\bar{\Delta}_1|^2 = \sum [\Delta(t) - \langle \Delta(t) \rangle_t]^2$, where the summation is over all the samples in t . Thus equation (D3) gives the usual formula for the standard deviation in this special case.

Next we consider another example, in which the spectrum again contains two incoherent components, the DC and a spectrally white component, but now this white component has a cutoff at frequency ω_c that is less than the Nyquist sampling frequency. In this case equation (D3) defines σ_{Δ}^2 as the power in the white component, $|\bar{\Delta}_1|^2$, divided by the reduced number of measurements, $2T\omega_c$. The usual formula for σ_{Δ}^2 always gives a lesser estimate than equation (D3) in this special case, and the estimate decreases in value as the sampling frequency increases while all other parameters remain fixed. On the other hand, σ_{Δ}^2 from equation (D3) remains constant for sampling that is greater than the cutoff frequency. The standard deviation given by equation (D3) thus correctly represents the fluctuation in a signal which is oversampled. This special case is relevant in our discussions concerning the effect of granulation evolution on the error in the determination of displacement, since it represents an oversampled fluctuating component.

REFERENCES

- Arrambide, M. R., Dunn, R. B., Healy, A. W., Porter, R., Widener, A. L., November, L. J., and Spence, G. E. 1983, in *Proc. Microdensitometry Conf. Astronomy* (Goddard Space Flight Center), ed. D. Klinglesmith, NASA Pub. 2317, p. 293.
 Brandt, P. 1988, *Nature*, submitted.
 Duvall, T. L., Jr. 1980, *Solar Phys.*, **66**, 213-221.
 Howard, R., Gilman, P. A., and Gilman, P. I. 1984, *Ap. J.*, **283**, 373.
 Leighton, R. B., Noyes, R. W., and Simon, G. W. 1962, *Ap. J.*, **135**, 474.
 Lindblad, B., and Brahe, R. 1946, *Ap. J.*, **104**, 211.
 Newton, H. W., and Nunn, M. L. 1951, *M.N.R.A.S.*, **111**, 413.
 November, L. J. 1984, in *Proc. Sacramento Peak Obs., Small-Scale Dynamical Processes in Quiet Stellar Atmospheres*, ed. S. L. Keil, (Sunspot, NM: AURA), p. 74.
 ——. 1986, *Appl. Optics*, **25**, 392.
 ——. 1988, *J. Opt. Soc. Am.*, **5**, 351.
 November, L. J., Simon, G. W., Tarbell, T. D., Title, A. M. and Ferguson, S. H. 1987, in *Proc. 2nd Workshop on Theoretical Problems in High-Resolution Solar Physics*, ed. G. Athay (NASA Conf. Pub. 2983), p. 121.
- November, L. J., Toomre, J., Gebbie, K. B., and Simon, G. W. 1981, *Ap. J. (Letters)*, **245**, L123.
 Simon, G. W., and Leighton, R. 1964, *Ap. J.*, **140**, 1120.
 Simon, G. W. 1967, *Zs. Ap.*, **65**, 345.
 Simon, G. W., et al. 1988, *Ap. J.*, **327**, 967.
 Stauffer, F. R., Smith, G. H., Streander, G. W., Wilkins, L. M., November, L. J., and Smartt, R. N. 1983, in *Proc. Los Alamos Conf. Optics*, ed. R. S. McDowell and S. C. Stotlar (Proc. SPIE, **290**, p. 77).
 Strömgren, G. 1946, *Ap. J.*, **104**, 12.
 Title, A. M., et al. 1987, *Adv. Space Res.*, **6B**, No. 8, 253.
 Title, A. M., Tarbell, T. D., Shine, R. A., Topka, K. P., and Ferguson, S. H. 1988, *Ap. J.*, submitted.
 von der Lühe, O. 1985, *Lecture Notes in Physics*, Vol. 233, ed. R. Müller (Berlin: Springer-Verlag), p. 62.
 Ward, F. 1965, *Ap. J.*, **141**, 534

LAURENCE J. NOVEMBER: National Solar Observatory/Sacramento Peak Sunspot, NM 88349

GEORGE W. SIMON: Air Force Geophysics Laboratory National Solar Observatory/Sacramento Peak Sunspot, NM 88349

Distribution /	
Availability Codes	
Dist	Avail and/or Special
A-1	2C

